Modeling and experimental validation of dynamical effects in Bragg coherent x-ray diffractive imaging of finite crystals

Yuan Gao,[1,*] Xiaojing Huang,[1] Ross Harder,[2] Wonsuk Cha,[2] Garth J. Williams,[1,†] and Hanfei Yan[1,‡]
[1]*National Synchrotron Light Source II, Brookhaven National Laboratory, Upton, New York 11973, USA*
[2]*Advanced Photon Source, Argonne National Laboratory, Lemont, Illinois 60439, USA*

(Received 6 September 2022; revised 8 November 2022; accepted 15 November 2022; published 30 November 2022)

Bragg coherent diffractive imaging (BCDI) is a noninvasive microscopy technique that can visualize the shape and internal lattice deviations of crystals with nanoscale spatial resolution and picometer deformation sensitivity. Its strain imaging capability relies on Fourier transform–based iterative phase retrieval algorithms, which are mostly developed under the kinematical approximation. Such approximation prohibits the application of BCDI on larger crystals, which are commonly seen in most emerging functional materials. Understanding the dynamical effect in BCDI, as well as developing a validated method for modeling BCDI at the dynamical diffraction limit, is crucial for applying BCDI to hierarchical systems that contain micron-sized crystals and grains. Here we report a comparative study on the impact of dynamical diffraction effects by comparing the reconstruction results from two measurements of the same crystal. Forward simulation is implemented to show subtle changes of interference fringes in the diffraction pattern due to the dynamical diffraction, and is compared directly with the experimental data.

DOI: 10.1103/PhysRevB.106.184111

I. INTRODUCTION

Strain can strongly influence the mechanical, chemical, and electronic properties of materials. Thus, precision measurement of crystal strain is a key challenge for characterizing and optimizing emergent functional materials. Hard x-ray Bragg coherent diffractive imaging (BCDI) has been demonstrated to be a very powerful tool for imaging lattice deformation in crystalline materials [1–6]. It provides a full-field–type imaging capability to map three-dimensional (3D) strain distribution in a micron-sized field of view with nanometer-scale spatial resolution and picometer-scale deformation sensitivity. In a typical BCDI measurement, a finite crystal is illuminated by a coherent x-ray beam, and the far-field 3D diffraction pattern in the vicinity of a single Bragg reflection is recorded with a spatial sampling rate beyond the Nyquist limit. The acquired 3D diffraction pattern is inverted to a complex object function using phase retrieval algorithms. Traditionally, the amplitude of the reconstructed object function indicates the scattering density distribution of the crystal, while the phase represents a projection of the deformation field to the momentum transfer vector of the measured Bragg peak.

Most BCDI phase retrieval algorithms [7–9] are developed under the kinematical approximation, in which the dynamical effects—-namely, multiple scattering and extinction—-are neglected. With such simplification, the far-field diffraction intensity from a finite crystal is the modulus square of the 3D Fourier transform (FT) of its effective electron density and deformation field, while the inverse FT of the far-field intensity provides an autocorrelation of the object. Therefore, the phase problem can be efficiently solved via FT-based iterative optimization algorithms, using *a priori* knowledge that the object being imaged is isolated. Such phase retrieval algorithms have been successfully applied to various systems, where sizes of measured crystals are typically in the range from a few hundreds of nanometers to approximately 1 μm. For larger crystals, those algorithms do not provide a simple map of the electron density, since the kinematical approximation is not valid anymore. Applying established FT-based algorithms on Bragg diffraction patterns from lager crystals will cause significant artifacts in both amplitude and phase of the reconstructed complex object functions [10].

Theoretically, the dynamical effects can be neglected if the size of a crystal is smaller than the x-ray extinction length [11,12]. However, in practice, it is difficult to predict whether a crystal can be treated under the kinematical approximation, since the extinction length of x-ray photons in a particular crystal could change significantly due to the lattice deformation field. For example, the extinction length of [111] Bragg diffraction at a photon energy of 9 keV is about 0.25 μm in a perfectly ordered gold or lead crystal [13]. However, micron-sized gold and lead crystals have been successfully imaged without any significant artifacts, using BCDI and FT-based phase retrieval algorithms [2,3,14]. The kinematical approximation is still valid in those large crystals, because of residual lattice deformations associated with the sample preparation. Without knowing the ground truth, one could easily confuse the artifacts from dynamical effects with actual features in a crystal far from equilibrium with its environment. Therefore, developing a wave propagation method that accommodates dynamical effects, as well as the corresponding phase retrieval approach, is crucial for applying BCDI on large crystals.

*yuangao@bnl.gov
†gwilliams@bnl.gov
‡hyan@bnl.gov

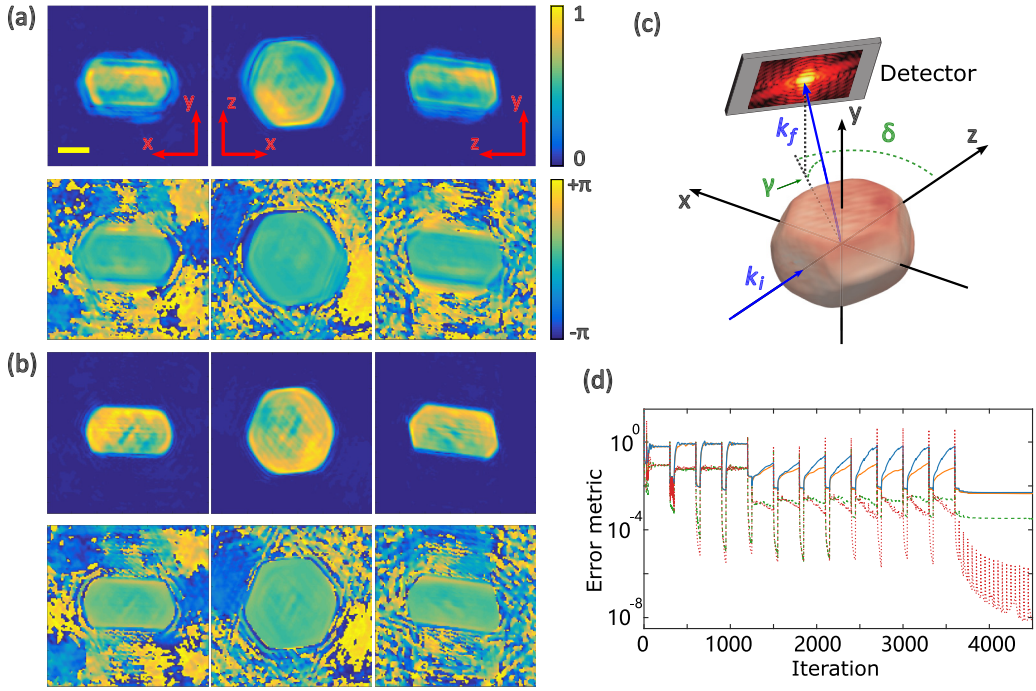

FIG. 1. Reconstruction from the [002] peak at 7.5 keV. The diffraction data were first inverted using an intentionally loosened support (a) and then using a fixed support (b). The scale bar is 250 nm. For both (a) and (b), slices of amplitude (top row) and phase (bottom row) are plotted, where the left, middle, and right columns are the slices along x-y, x-z, and y-z planes, respectively. The definition of diffraction geometry is shown in (c). $\boldsymbol{k}_i$ and $\boldsymbol{k}_f$ are the wavevectors of incident and diffracted x-ray photons, respectively. The laboratory coordinate is right-handed, where y is upward, and z is the propagation direction of the incident x-ray beam. δ and γ are the detector angles. (d) Error metrics during the iterative phase retrieval. χ^2 of the first (blue) and second (amber) trials, as well as the corresponding η^2 (green and red, respectively), are plotted in logarithmic scale.

Dynamical effects can be described in the frame of x-ray dynamical diffraction theory, which has been extensively developed for decades [11,15–17]. Works have been done to investigate the impact of dynamical diffraction effects on transmitted beams [18,19] and extended samples [20]. More recently, Yan and Li [21] and Shabalin *et al.* [22] have applied the theory on finite crystals to simulate the coherent diffraction patterns. The latter group also simulated BCDI on a hemispherical lead particle using the same diffraction geometry and a similar crystal dimension described in Ref. [3]. While both works provide valuable insight into the impact of dynamical effects on BCDI, none of them has validated the simulations against experimental data. In this work, we perform BCDI measurements of the same crystal at two energy points to illustrate the impact of dynamical diffraction effects in the reconstruction, and use forward simulation to validate subtle changes observed in the diffraction pattern associated with different diffraction modes against experimental data.

II. BCDI DATA COLLECTION AND PHASING

A. BCDI sample preparation and data collection

The gold crystal sample was prepared by dewetting evaporated gold films at a temperature just below melting [1]. The target crystal was selected based on its dimension and the estimated x-ray extinction length. According to the database [13], the extinction length in a perfectly ordered gold crystal is about 0.25 μm for [002] reflection and approximately 0.70 μm for [004] reflection. The extinction length is calculated assuming a sigma-polarized incident wave. Details about estimation of the extinction length are discussed in Appendix A. Considering the presence of deformation, these numbers could be larger in a real crystal. Therefore, we selected a crystal that has a size of approximately 700 nm in diameter and 350 nm in height. Given its dimensions, the [004] diffraction patterns measured from this crystal should be inverted correctly using algorithms developed under the kinematical approximation, while reconstructions from [002] datasets are expected to show significant artifacts due to dynamical diffraction effects. In a later section, the reconstruction from [004] reflection serves as the crystal model to perform forward simulation, while the [002] reflection is used as the reference to validate the simulation results.

The BCDI experiment was conducted at beamline 34-ID-C of the Advanced Photon Source, Argonne National Laboratory. The dataset of [002] reflection was collected at a photon energy of 7.5 keV, and [004] reflection was collected at 15 keV. The two reflections were measured using identical diffraction geometry, where a pixelated detector with 55 $\mu m \times 55\ \mu m$ pixels was orientated at $\delta = 41.40^\circ$ and $\gamma = 26.55^\circ$ (as shown in Fig. 1). The crystal was rotated around the y-axis during rocking scans using a rocking step of 6 mdeg for [002] reflection and 3 mdeg for [004] reflection. The sample–detector distance was fixed at 1.5 m. As a result, the sampling rate of [004] reflection is slightly below the ideal condition, while the spatial resolution of reconstructions from

the [002] reflection is reduced due to the limitation in the largest scattering angle.

B. BCDI phase retrieval

The collected diffraction data sets were inverted using the established error reduction (ER) and hybrid input–output (HIO) algorithms [7]. All the phasing processes were initialized using random seeds and a support size of 80% of the input array. A total of 4500 iterations were carried out for each phasing trial. The first 3600 iterations were switched between 50 iterations of ER and 250 iterations of HIO to approach the global minimum. The following 900 iterations were performed with ER only to refine the converged solution. Considering the large crystal size and limited beam coherence length, an iterative blind deconvolution method—namely the Richardson-Lucy (RL) algorithm [23,24]—was adopted to separate the beam coherence function from the estimate of the diffracted wavefield [25]. The coherence function was updated every 50 iterations starting with the 1200th iteration, with RL algorithm runs for 20 iterations per update. The final object was obtained by averaging over the estimated objects resulting from every other iteration in the last 100 iterations.

Due to the absorption and extinction effects, part of the reconstructed complex object may have a much weaker amplitude, which has been discussed in previous theoretical studies [10,22]. Therefore, the regular shrink-wrap [26] method often cannot constrain the support correctly, resulting in a cavity- or pit-like artifact in the final reconstruction. To avoid this problem, we used an alternative approach to shrink the support at a controlled speed. In this approach, the 3D dimensions of support are reduced by a certain number of voxels with a specified interval of iterations, and the shrinking stops where the boundary of the support touches the boundary of the estimated object, determined by a predefined threshold. This method allows the algorithms to find the correct solution before stagnating around a local minimum due to an overtightened support.

Figure 1 demonstrate the reconstruction and the corresponding error metrics of 7.5-keV data. To avoid the potential risk of overtightening the support, the threshold for determining the edge of crystal was set to approximately 5% in the first trial of phase retrieval. The resultant amplitude and phase of the retrieved object function are shown in Fig. 1(a). Although the boundary of the crystal can be easily distinguished by eye, the region between the edge of the intentionally loosed support and the edge of the crystal contains voxels with relatively large amplitudes. To get a clean morphology of the crystal, we conducted a second trial of phase retrieval using a fixed support that was obtained by thresholding the first reconstruction followed by manual modification. The fixed-support phase retrieval gave a reconstruction with a well-defined crystal boundary. Figure 1(b) shows slices of amplitude of the retrieved object function along the three axes of the lab frame Cartesian coordinate. As the x-ray wave was incident along $+z$-axis and diffracted in the outboard–upward direction, the downstream part of the crystal has a lower amplitude compared to the remaining part. The corresponding slices of the phase demonstrate nonphysical artifacts that are spatially correlated to the low-amplitude part, suggesting that they originated from the absorption and extinction effects of the x-rays. It is also worth noting that the phase artifacts are not linearly proportional to the optical path of the x-ray inside the crystal, indicating the presence of the extinction effect [10]. Two error metrics were used to monitor the convergence of the phase retrieval algorithm. Besides the traditional reciprocal-space χ^2 error metric, an η^2 error metric was used to measure the iteration-to-iteration variation. η^2 is defined as

$$\eta^2 = \frac{|\mathcal{F}(o_n) - \mathcal{F}(o_{n-1})|^2}{|\mathcal{F}(o_{n-1})|^2},$$

where o_n is the estimate of the complex object on the nth iteration. Figure 1(d) demonstrates the error metrics during two phase retrieval trials. Both trials have final χ^2 values below 10^{-2}, suggesting a reliable phase retrieval result. The second trial ends at a slightly higher χ^2 value, which is likely due to fixing the support. As for the η^2 values, the first trial stagnates around 10^{-3} during the last 900 iterations of ER, indicating the algorithm was trapped in a local minimum due to the intentionally loosed support. As a comparison, the second trial was able to converge to a consistent result, with a final η^2 value below 10^{-8}.

The same phase retrieval procedure was used for the 15-keV dataset, i.e., a loosed-support phase retrieval followed by a fixed-support one. As mentioned previously, the extinction length of [004] diffraction from a perfectly ordered gold crystal is about 0.70 μm, similar to or larger than the dimensions of the crystal we measured. Therefore, we estimated that the kinematical approximation is still valid for the 15-keV dataset. The result of phase retrieval confirmed this estimation. Figure 2(a) shows only the amplitude and phase of the object reconstructed using a fixed support. Comparing with the 7.5-keV dataset, the reconstruction from 15-keV dataset has an almost identical morphology, with a relatively smooth amplitude distribution inside the crystal boundary, as expected. The corresponding phase maps show a smooth distribution in the center part of the crystal, while the region near the boundary has an approximately 1.2-radian phase ramp relative to the center. This indicates the presence of lattice displacement in the surface layers of the crystal, which has been discussed in previous studies [2,14]. The corresponding χ^2 and η^2 error metrics [see Fig. 2(b)] have final values below 10^{-2} and 10^{-8}, respectively, which are as good as the second trial of 7.5-keV case.

III. FORWARD SIMULATION OF DYNAMICAL DIFFRACTION

In the first part of this section, we briefly describe the formulism used for propagating the x-ray wave field through a crystal in the dynamical diffraction regime. Then, the crystal model reconstructed from the 15-keV dataset is used as the ground truth to simulate the far-field diffraction patterns of two Bragg peaks at corresponding photon energies. The simulation results are validated by a direct comparison with the experimental data.

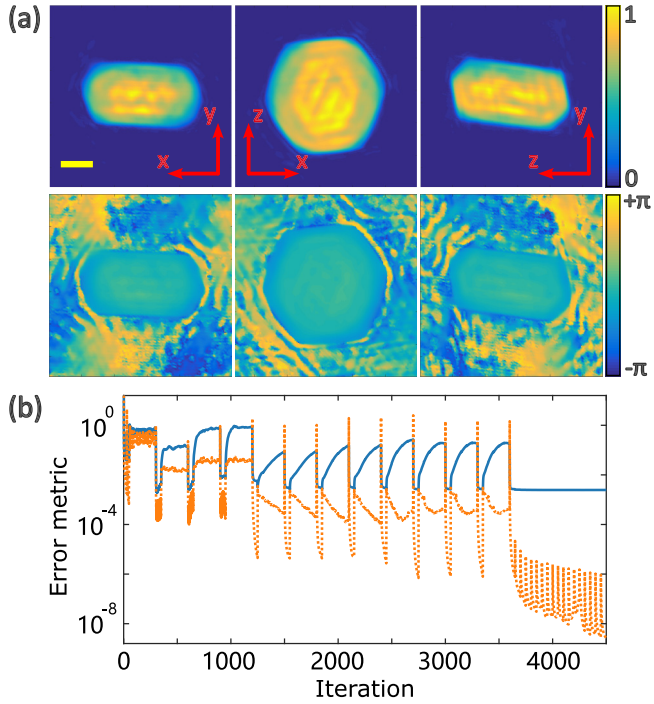

FIG. 2. Reconstruction from the [004] peak at 15 keV. The diffraction data were inverted following the same two-step procedure. The result using a fixed support is shown in (a). The scale bar is 250 nm. Slices of amplitude (top row) and phase (bottom row) are demonstrated, where the left, middle, and right columns are the slices along x-y, x-z, and y-z planes, respectively. Error metrics—χ^2 (blue) and η^2 (amber)—during the phase retrieval with fixed support are plotted in logarithmic scale in (b).

A. Dynamical diffraction formulism

The simulation method used in this work is developed based on the study conducted by Yan and Li [21], with some modifications inspired by Ref. [22]. The propagation and interaction of wavefields inside a crystal, as well as the absorption and refraction effects, are described by the Takagi-Taupin equations [15,16]. Following Refs. [21], [22], and [27], the crystal wave with two-beam approximation can be written as

$$\frac{\partial D_0}{\partial s_0} = \frac{ik}{2}(\chi_0 D_0 + \chi_{\bar{h}} D_h)$$
$$\frac{\partial D_h}{\partial s_h} = \frac{ik}{2}\left\{\chi_h D_0 + \left[1 + \chi_0 - \frac{k_h^2}{k^2} + \frac{2}{k}\frac{\partial(\boldsymbol{h}\cdot\boldsymbol{u})}{\partial s_h}\right] D_h\right\}, \quad (1)$$

where $\hat{\boldsymbol{s}}_0$ and $\hat{\boldsymbol{s}}_h$ are the unit vectors along the transmitted wave, $D_0(\boldsymbol{r})\exp(i\boldsymbol{k}_0\cdot\boldsymbol{r})$, and diffracted wave, $D_h(\boldsymbol{r})\exp(i\boldsymbol{k}_h\cdot\boldsymbol{r} - i\boldsymbol{h}\cdot\boldsymbol{u})$, respectively; $k = \frac{2\pi}{\lambda}$ is the wavevector of the x-ray, and $\boldsymbol{k}_0 = k\hat{\boldsymbol{s}}_0$, $\boldsymbol{k}_h = \boldsymbol{k}_0 + \boldsymbol{h} = k_h\hat{\boldsymbol{s}}_h$; $\boldsymbol{h}$ is the reciprocal lattice vector of the unstrained crystal; $\boldsymbol{u}$ is the displacement vector; and χ_0, χ_h, and $\chi_{\bar{h}}$ are Fourier coefficients of the susceptibility function of the crystal.

Equation (1) includes coupled partial–differential equations and can only be solved analytically in some particular cases [12]. For a general case, it is necessary to integrate the equations numerically. An iterative process is developed to solve Eq. (1) numerically. For an incident wave

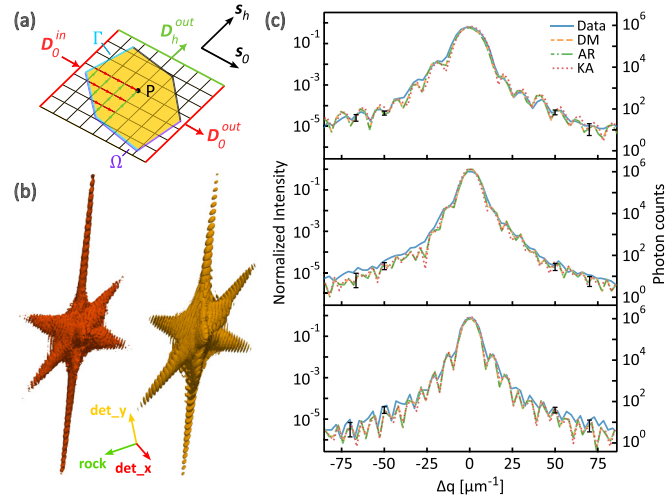

FIG. 3. Forward simulation of the [004] peak at 15 keV. (a) Schematic of x-ray diffraction from an arbitrary crystal. $\boldsymbol{s}_0$, $\boldsymbol{s}_h$ represent the directions of transmitted and diffracted waves, respectively. Boundary conditions must be satisfied on Γ (blue) for the transmitted wave and on Ω (purple) for the diffracted wave. The wavefield at an arbitrary voxel P inside the crystal is integrated from all upstream voxels, as marked by red and green arrows. (b) 3D diffraction intensity of experimental data (left) and forward simulation from the DM (right), plotted in the detector frame. (c) Line intensity variations across the center of 3D diffraction intensity: along the y-axis (top) and x-axis (middle) of the detector, and the rocking axis (bottom). Simulation results from the DM (amber), AR (green), and KA (red) are normalized to the experimental data (blue) by integrated intensity, and then aligned using cross-correlation. Black error bars represent the Poisson noise of the DM simulation at ±50 and ±70 μm^{-1}, respectively.

$\psi_0(\boldsymbol{r})\exp(i\boldsymbol{k}_0\cdot\boldsymbol{r})$, at the nth iteration, the transmitted and diffracted waves at an arbitrary point (s_0, s_h) on an $\hat{\boldsymbol{s}}_0$, $\hat{\boldsymbol{s}}_h$ slice of the crystal [see Fig. 3(a)] can be obtained,

$$D_0^{(n)}(s_0, s_h) = D_0\left(s_0^{\Gamma}, s_h\right)\exp\left[ic_0\left(s_0 - s_0^{\Gamma}\right)\right] + ic_{\bar{h}}\int_{s_0^{\Gamma}}^{s_0} D_h^{(n-1)}(s_0', s_h)\exp[ic_0(s_0 - s_0')]ds_0' \quad (2)$$

and

$$D_h^{(n)}(s_0, s_h) = ic_h\int_{s_h^{\Omega}}^{s_h} D_0^{(n)}(s_0, s_h')\exp\{i\boldsymbol{h}\cdot[\boldsymbol{u}(s_0, s_h) - \boldsymbol{u}(s_0, s_h')] + ic_w(s_h - s_h')\}ds_h', \quad (3)$$

where $c_{0,h,\bar{h}} = \frac{1}{2}k\chi_{0,h,\bar{h}}$ and $c_w = \frac{1}{2}k(1 + \chi_0 - k_h^2/k^2)$. The integrations use boundary conditions $D_0(s_0^{\Gamma}, s_h) = \psi_0(s_0^{\Gamma}, s_h)$ and $D_h(s_0, s_h^{\Omega}) = 0$, where ψ_0 is the incident x-ray wave. As shown in Fig. 3(a), Γ and Ω are the upstream crystal boundaries of the transmitted and diffracted waves, respectively; s_0^{Γ} is the s_0 coordinate of Γ at s_h, and s_h^{Ω} is the s_h coordinate of Ω at s_0. The iteration starts by assuming $D_h^{(0)} = 0$, and continues until a converged solution emerges. The mathematical proof of convergence is detailed in Ref. [22].

For a specific diffraction geometry, Eqs. (2) and (3) are numerically solved for each $\hat{\boldsymbol{s}}_0$, $\hat{\boldsymbol{s}}_h$ slice of the crystal to

obtain D_h at the exit boundary of the crystal, yielding a two dimensional (2D) wavefront at the exit crystal surface of the diffracted beam. Such an exit wavefront is propagated to the far field using 2D FT, and the resultant modulus represents the diffraction pattern recorded by a pixelated detector. To simulate a rocking curve scan, the process just described is repeated at each rocking angle.

It is worth mentioning that Eqs. (2) and (3) can also accommodate diffraction with only the absorption and refraction effects—i.e., ignoring the extinction effect—and the situation at the kinematic limit. One can easily see that the extinction effect is described by the second term on the right-hand side of Eq. (2): the D_0 propagated from the incident surface Γ to a point (s_0, s_h) is further attenuated due to the presence of nonzero D_h on the propagation path. To neglect this effect, we can simply take the D_h obtained from the first iteration and propagate it to the far field. As for the situation at the kinematic limit, not only is the extinction effect neglected, but also the susceptibilities $\chi_{0,h,\bar{h}}$ are set to very small nonzero values. In this case, D_h in Eq. (3) is simply a function of $\int D_0(\boldsymbol{r}) \exp[i\boldsymbol{h} \cdot \boldsymbol{u}(\boldsymbol{r})] d\boldsymbol{r}$, which is the well-known formula of kinematical diffraction.

B. Forward simulation of the [004] peak

As mentioned earlier, the [004] diffraction should not see a significant dynamical effect, since the estimated extinction length is comparable to or even larger than the dimension of the crystal. Therefore, we start with the simulation of the [004] diffraction at 15 keV to establish the baseline.

The reconstruction from the 15-keV dataset was used as the model for forward simulation. As shown in Fig. 2(a), the amplitude of the reconstructed object contains obvious modulations. These modulations are commonly seen in BCDI and are usually attributed to numerical errors induced by the FT-based iterative phase retrieval. To remove such nonphysical features, the amplitude inside the crystal was set to one, where the crystal boundary was determined by an isosurface level of 20%.

Three types of far-field diffraction patterns were calculated: a dynamical diffraction model (DM), a kinematical diffraction model with absorption and refraction effects (AR), and a pure kinematical diffraction model (KA). The simulations were normalized using integrated intensity of the experimental data. All simulated diffraction patterns were aligned to the data by minimizing the cross-correlation coefficient between each pair of 3D diffraction patterns.

Figure 3 demonstrates the experimental data and results of all three models. Logarithmic-scale line intensity variations across the center of the Bragg peak are plotted along the three axes of diffraction patterns in the detector frame, as shown in Fig. 3(c). As expected, simulations from three models show very similar intensity profiles, since the effects of absorption, refraction, and extinction are negligible for this particular reflection. Compared to the data, all three models correctly reproduce the measured intensity distribution down to the order of 10^{-4}, with well-matched interference fringes. The simulations slightly differ from the data in the high-q region, especially for where the relative intensity is less than 10^{-4} of the center of the Bragg peak. This phenomenon is discussed later.

Besides the inconsistency in the high-q region, simulations also show better fringe visibility when compared with the data. This is likely an effect of the limited coherence of the incident x-ray beam, since the simulations were conducted assuming the crystal is illuminated by a fully coherent beam. Although this partial coherence effect has been separated from the reconstructed object via blind deconvolution during the phase retrieval process, it cannot be added back by a simple convolution in the forward simulation. Technically, the diffraction with a partially coherent beam should be simulated by considering all major coherent modes of the beam [28,29]. However, understanding the coherence property of source at 34-ID-C, as well as performing and validating the decomposition of coherent modes, are out of the scope of this work. Therefore, the partial coherent effect is not accommodated in forward simulations presented herein.

C. Forward simulation of the [002] peak

Simulation of [002] diffraction at 7.5 keV was conducted using the same method described earlier. Similarly, three diffraction models were calculated. It is important to note that the crystal model is retrieved from the [004] dataset since it is more error free and closer to the ground truth. The phase of the reconstructed complex object function represents $\boldsymbol{h}_{[004]} \cdot \boldsymbol{u}$. When simulating [002] diffraction, the phase needs to be divided by two to match the momentum transfer vector $\boldsymbol{h}_{[002]}$.

Simulations were normalized and aligned to the experimental data using the procedure described in the previous section. In Fig. 4, logarithmic-scale line intensity variations of the simulated diffraction patterns are plotted against the measured diffraction data. Unlike [004], the KA result of [002] is significantly different from those of DM and AR. Such differences suggest that absorption, refraction, and extinction effects play important roles in this reflection.

Compared to the data, all models accurately reproduce the height and width of the center peak, but show different performances in the side lobes. Along the horizontal axis of the detector [Fig. 4(b)], results from all three models show interference fringes with periodicities and relative intensities similar to the data. The DM shows a slightly better consistency, especially on the $+\Delta$q side of the center peak. Like the [004] case, the fringe visibilities of simulated results are better than the data, which can be attributed to the effect of partial coherence. Along the vertical axis of the detector [Fig. 4(a)], different levels of consistency are observed on the $+\Delta q$ side and $-\Delta q$ side. On the $+\Delta q$ side, the relative intensities of side lobes from the DM and KA are very similar to those of the data, except for the second and fifth orders. For the AR, the first-order side lobe has a relative intensity that is 30% lower than that of the experimental data, indicating it cannot reproduce the relative intensity accurately. On the $-\Delta q$ side, the relative intensities of the side lobes calculated from the KA are significantly weaker than those of the data by 50% or more. The first two side lobes of the AR have similar relative intensities as the data, but the third order is as weak as the one from the KA. As a comparison, the DM correctly reproduces

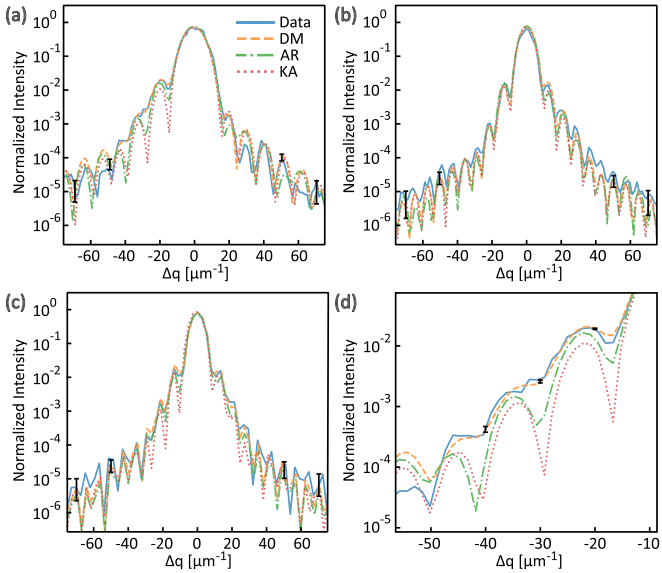

FIG. 4. Forward simulation of the [002] peak at 7.5 keV. Line intensity variations from experimental data (blue), DM (amber), AR (green), and KA (red) are plotted across the center of 3D diffraction intensity, along (a) y-axis and (b) x-axis of the detector, and (c) the rocking axis. Black error bars represent the Poisson noise of the DM simulation at ± 50 and $\pm 70\ \mu m^{-1}$, respectively. (d) Detail of the first few orders of side lobes on the $-\Delta q$ side from data shown in (a). Black error bars represent the Poisson noise of the DM simulation at -20, -30, and $-40\ \mu m^{-1}$, respectively.

the intensities of the first three orders of the side lobes, down to a relative intensity as low as 10^{-4}. Higher order side lobes of the DM simulation do not match the data very well, which is discussed in the next section.

Besides the visual inspection, we also calculated the χ^2 error metric between the data and simulations. The χ^2 values are 0.047 for the DM, 0.064 for the AR, and 0.121 for the KA. Both the DM and AR have significant lower χ^2 values than the KA, suggesting that most of the subtle changes in the side lobes are caused by the absorption and refraction effects. Meanwhile, the DM's error is slightly better than the AR, indicating that the extinction effect also plays an important role in this reflection. As a comparison, for the [004] reflection at 15 keV, the χ^2 values are 0.081, 0.080, and 0.167 for the DM, AR, and KA, respectively. While the absorption and refraction effects are still important for [004] reflection, the difference caused by the extinction effect is negligible.

IV. DISCUSSION

As mentioned earlier, simulations using the DM can accurately reproduce the intensity distribution in the low-q region, but a difference in the high-q region is still observed. This is mostly caused by two factors. First, because of the well-known Q^{-4} power law decay of the diffraction signal [30], the measured diffraction data have many fewer photon counts in the high-q region. Such low counts result in a much higher uncertainty of measurement—namely, the Poisson noise—as demonstrated by the error bars in Figs. 3(c) and 4. The weak signal is also more susceptible to background noise like scattering from alien scatterers [31]. Since we did not add any noise to the simulated diffraction patterns, it is not surprising that the simulations and data are inconsistent in the high-q region. Second, we do not know the ground truth, and the reconstructed crystal from the [004] dataset could still contain artificial fine structures because of the noisy high-q data. Forward simulations from such an imperfect crystal model would inherently cause inconsistency in the high-q region when compared with experimental data.

Besides the differences in high-q region, simulations also show a mismatch at some specific momentum transfer values. For example, as shown in Fig. 4(a), the second side lobe on the $+\Delta q$ side always has a much higher relative intensity when comparing simulations to the data. Although the actual cause is unclear, a mismatch at a specific momentum transfer value usually indicates the real space object contains artifacts with the corresponding spatial frequency. Our hypothesis is that the FT-based phase retrieval process introduces numerical errors with certain spatial frequencies. As shown in Fig. 2(a), not only the amplitude of the reconstructed object function contains unphysical modulations, but also the phase term shows visible modulations that are spatially correlated to those in amplitude. The modulations in amplitude have been removed before performing forward simulations, based on a physical assumption that the effective electron density of the crystal is uniform. The phase artifacts, however, cannot be corrected without knowing the ground truth. A potential solution to this problem is performing phase retrieval with constrained amplitude variation. Such an additional constraint might force the algorithm to find a solution with uniform amplitude distribution and eliminate the nonphysical modulations in phase.

From the reconstruction of [002] shown in Fig. 1(a) and (b), as well as the previous theoretical studies [10,22], we can see that both the absorption/refraction effect and the extinction effect can cause the low-intensity region in the amplitude map and the corresponding phase artifacts. However, these two effects have different impacts in practice. The absorption/refraction effect induces artifacts that are linearly proportional to the optical path of x-ray inside the crystal. Such artifacts can be identified and corrected numerically after the phasing process, since the FT-based mathematical model is still valid [10]. As a comparison, extinction effects usually induce nonlinear artifacts due to the fact that 3D Fourier transform is no longer sufficient to describe the physical process. Without knowing the ground truth, it is very difficult or almost impossible to distinguish the extinction-induced artifacts from actual deformations in the crystal. The forward simulation method described herein can serve as a validation tool to evaluate the severity of the issue. By comparing simulated diffraction patterns from kinematical and dynamical models with measured ones, as well as the reconstructions from various models and measured data (as shown in Appendix B), we can verify whether the reconstruction result is free from dynamical artifacts.

V. CONCLUSION

In summary, we performed BCDI measurements at two energy points on the same gold crystal to evaluate the impact of dynamical diffraction in the reconstruction. They correspond

to two scenarios: one where the extinction length is much less than the dimension of crystal, and the other where the extinction length is comparable to the dimension of crystal. For the former scenario, both dynamical and kinematical models produce similar 3D diffraction intensity consistent with measured data, suggesting that the dynamical effects are negligible. For the latter scenario, simulation using the dynamical diffraction model reproduces more accurately the subtle changes of the interference fringes in the experimental data, which cannot be achieved using the kinematical approach. We show that these subtle changes in the diffraction pattern can lead to an erroneous reconstruction result with an FT-based phase retrieval algorithm. To alleviate the dynamical artifact, a high-index reflection with a bigger extinction depth would be preferred. The forward reconstruction simulation method proposed here can be used as a cross-validation tool to assess the correctness of FT-based models. Although at the current stage a quantitative correction removing the dynamical artifacts has not been achieved, the iterative nature of the forward modeling makes it possible to be incorporated into the iterative optimization algorithm in the future to accommodate dynamical diffraction effects in BCDI phase retrieval. Such an algorithm will enable BCDI on hierarchical systems that contain large crystalline grains and domains, which are commonly seen in emerging functional materials like additive manufactured metals, single-crystal cathode materials, and photonic nanostructures. Quantitively mapping strain in these systems is essential for understanding and optimizing their functional properties.

ACKNOWLEDGMENTS

This research used resources of the National Synchrotron Light Source II, a U.S. Department of Energy (DOE) Office of Science user facility operated for the DOE Office of Science by Brookhaven National Laboratory under Contract No. DE-SC0012704. The data for x-ray diffraction experiments were collected at the Microdiffraction and Coherent X-ray Scattering beamline 34-ID-C at the Advanced Photon Source, a U.S. DOE Office of Science user facility operated for the DOE Office of Science by Argonne National Laboratory under Contract No. DE-AC02-06CH11357.

APPENDIX A: ESTIMATION OF EXTINCTION LENGTH IN A FINITE CRYSTAL

In this work, the extinction length in a finite crystal is estimated by calculating the extinction depth in a perfectly ordered crystal, considering the symmetric case of Bragg geometry. The extinction depth is defined as the depth along the normal direction of the surface at which the transmission intensity decreased to $1/e$. According to Ref. [12], the extinction length in Bragg geometry is

$$L_{\text{ext}}^{\text{Bragg}} = \frac{\lambda\sqrt{\gamma_0|\gamma_h|}}{Re(\sqrt{\chi_h\chi_{\bar{h}}})},$$

where $\gamma_{0,h}$ are the direction cosines and $\chi_{h,\bar{h}} = \chi_{rh,r\bar{h}} + i\chi_{ih,i\bar{h}}$ are the Fourier components of the dielectric susceptibility.

TABLE I. Extinction depths of [002] and [004] reflections at 7.5 keV and 15 keV, respectively.

		Symmetric, Bragg geometry extinction depth (μm)	
Au	Reflection	σ-polarized	π-polarized
7.5 keV	[002]	0.251	0.374
	[004]	0.706	2.245
15 keV	[002]	0.251	0.273
	[004]	0.703	1.047

Considering the symmetric case, the extinction depth is

$$L_{\text{ext}}^{\text{Bragg}} = \frac{\lambda\sin\theta_B}{Re(\sqrt{\chi_h\chi_{\bar{h}}})},$$

where θ_B is the Bragg angle. Also from Ref. [12], there is

$$Re(\sqrt{\chi_h\chi_{\bar{h}}}) = |\chi_{rh}| = \frac{R\lambda^2 F_{rh}}{\pi V},$$

where R is the classical radius of the electron, $F_h = F_{rh} + iF_{ih}$ is the structure factor, and V is the volume of the unit cell. Combining these two equations, we have

$$L_{\text{ext}}^{\text{Bragg}} = \frac{\lambda\sin\theta_B}{Re(\sqrt{\chi_h\chi_{\bar{h}}})} = \frac{\pi V\sin\theta_B}{\lambda R F_{rh}} \sim \frac{1}{d},$$

where Bragg's law $\lambda = 2d\sin\theta_B$ is used. From this equation, we can see that for the symmetric case in Bragg geometry, if the photon energy is not very close to the absorption edge, the extinction depth has a linear dependence to $1/d$.

The extinction depths of the [002] and [004] reflections at two photon energies in a perfectly ordered gold crystal are listed in Table I. We can see that the [002] reflection at 7.5 keV and the [004] reflection at 15 keV have the identical diffraction geometry but significantly different extinction depths. Therefore, we are able to tune the ratio between the extinction depth and the crystal size, without changing the sample crystal or the diffraction geometry.

APPENDIX B: PHASE RETRIEVAL OF SIMULATED DATA WITH DIFFERENT MODELS

To understand more fully the impact of absorption, refraction, and extinction effects on a reconstruction from diffraction data, we performed phase retrieval on diffraction data simulated using three models. The results are demonstrated in Fig. 5. For all phasing processes, 4500 iterations were carried out, while the first 3600 iterations alternated between 50 iterations of ER and 250 iterations of HIO, and the remaining 900 iterations were ER only.

Figures 5(a)–5(c) demonstrate reconstructed objects from the KA, AR, and DM, respectively, using the regular shrink-wrap approach with a Gaussian blurry function with a 1.0 pixel width and a 20% cutoff threshold. As a comparison, results shown in Figs. 5(d)–5(f) were retrieved using the two-step approach described in Sec. II B. Apparently, both approaches were able to invert the diffraction from the KA correctly, resulting in reconstructions very similar to the crystal model used for forward simulation [as shown in Figs. 5(a)

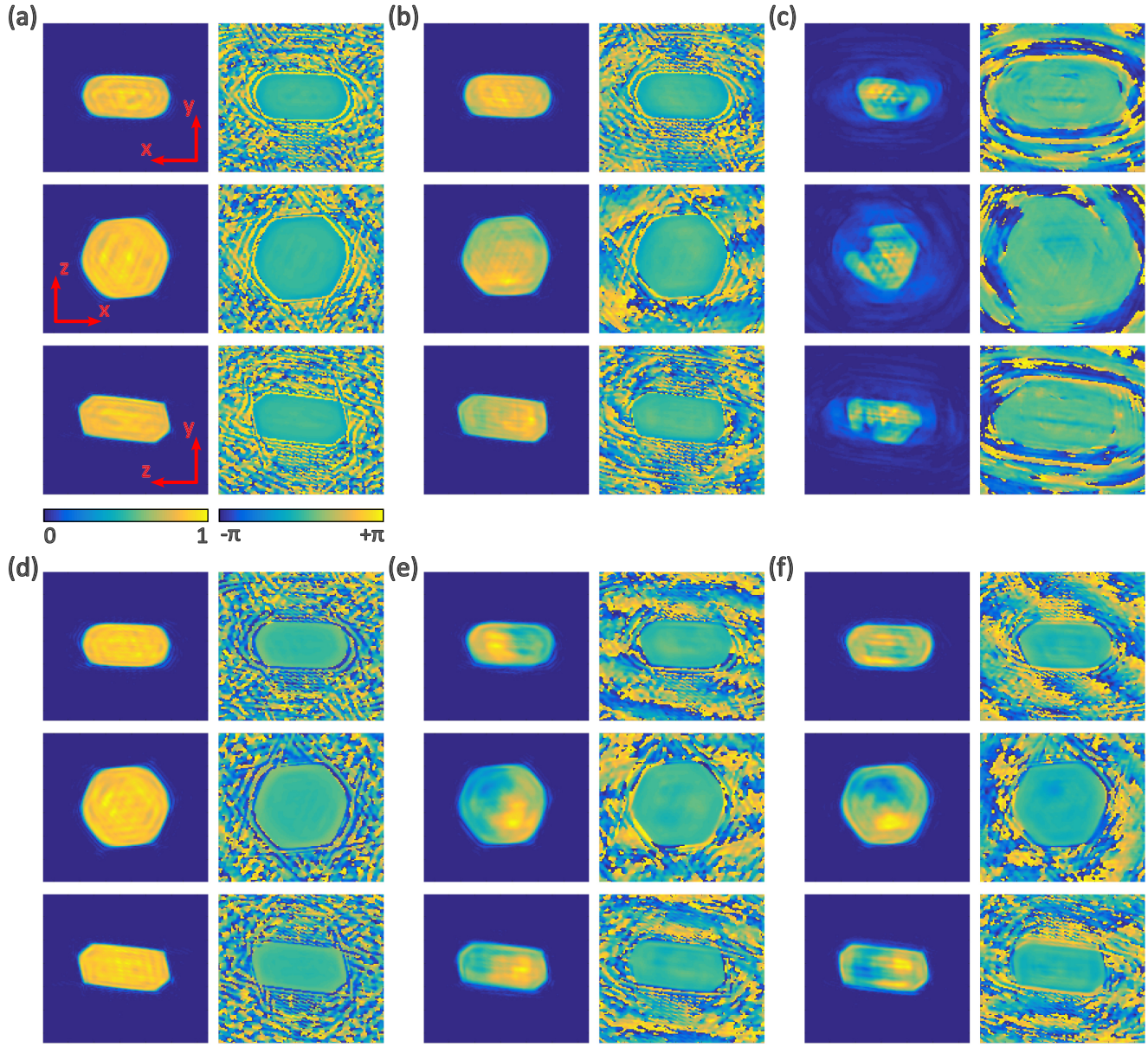

FIG. 5. Reconstructions from diffraction data simulated using different models. (a) and (d) are retrieved from KA, (b) and (e) are from AR, and (c) and (f) are from DM. The traditional shrink-wrap algorithm was used when inverting (a), (b), and (c), while (d), (e), and (f) were inverted using the two-step approach described in Sec. II B.

and 5(d)]. However, it is worth noting that both reconstructions contain amplitude modulations, while the crystal model has a flat amplitude distribution inside the crystal boundary.

Reconstructions from the AR simulation, as shown in Figs. 5(b) and 5(e), have a nonuniform amplitude distribution inside the crystal boundary due to the attenuation of the transmitted x-ray beam. The retrieved crystals are slightly different in shape. Specifically, the xz cross-section of the crystal inverted via the regular shrink-wrap approach [Fig. 5(b), middle] has an asymmetric, hexagonal shape, which is different from the crystal model used for the simulation. This can be attributed to the support that was overtightened by the shrink-wrap approach. While tweaking the parameters of the Gaussian blurry function might correct this problem, one could easily overlook such an inconsistency without knowing the ground truth. As a comparison, the two-step approach correctly retrieved the crystal shape.

For the DM simulation, phasing with the shrink-wrap approach was not able to obtain a reasonable crystal shape due to stagnation. The two-step approach, however, was still able to get the correct shape. Meanwhile, compared with the reconstruction of the AR simulation, which shows a relatively smooth phase, reconstruction of the DM simulation contains significant phase artifacts that are spatially correlated with the artifacts in amplitude distribution. In practice, such phase artifacts are likely to be interpreted as localized defects, while the ground truth or complementary information is lacking.

[1] I. K. Robinson, I. A. Vartanyants, G. J. Williams, M. A. Pfeifer, and J. A. Pitney, Reconstruction of the Shapes of Gold Nanocrystals Using Coherent X-ray Diffraction, Phys. Rev. Lett. **87**, 195505 (2001).

[2] G. J. Williams, M. A. Pfeifer, I. A. Vartanyants, and I. K. Robinson, Three-Dimensional Imaging of Microstructure in Au Nanocrystals, Phys. Rev. Lett. **90**, 175501 (2003).

[3] M. A. Pfeifer, G. J. Williams, I. A. Vartanyants, R. Harder, and I. K. Robinson, Three-dimensional mapping of a deformation field inside a nanocrystal, Nature (London) **442**, 63 (2006).

[4] I. Robinson and R. Harder, Coherent X-ray diffraction imaging of strain at the nanoscale, Nat. Mater. **8**, 291 (2009).

[5] A. Davtyan *et al.*, Threefold rotational symmetry in hexagonally shaped core–shell (In,Ga)As/GaAs nanowires revealed by coherent X-ray diffraction imaging, J. Appl. Crystallogr. **50**, 673 (2017).

[6] S. Labat *et al.*, Inversion domain boundaries in GaN wires revealed by coherent Bragg imaging, ACS Nano **9**, 9210 (2015).

[7] J. R. Fienup, Phase retrieval algorithms: A comparison, Appl. Opt. **21**, 2758 (1982).

[8] V. Elser, Phase retrieval by iterated projections, J. Opt. Soc. Am. A **20**, 40 (2003).

[9] S. Marchesini, A unified evaluation of iterative projection algorithms for phase retrieval, Rev. Sci. Instrum. **78**, 011301 (2007).

[10] W. Hu, X. Huang, and H. Yan, Dynamic diffraction artefacts in Bragg coherent diffractive imaging, J. Appl. Crystallogr. **51**, 167 (2018).

[11] B. W. Batterman and H. Cole, Dynamical diffraction of x rays by perfect crystals, Rev. Mod. Phys. **36**, 681 (1964).

[12] A. Authier, *Dynamical Theory of X-Ray Diffraction* (Oxford University Press, Oxford, 2003).

[13] S. A. Stepanov, in *Advances in Computational Methods for X-Ray and Neutron Optics*, edited by M. Sanchez Del Rio (SPIE Press, Bellingham, 2004), pp. 16–26,

[14] R. Harder, M. A. Pfeifer, G. J. Williams, I. A. Vartanyants, and I. K. Robinson, Orientation variation of surface strain, Phys. Rev. B **76**, 115425 (2007).

[15] S. Takagi, Dynamical theory of diffraction applicable to crystals with any kind of small distortion, Acta Crystallogr. **15**, 1311 (1962).

[16] D. Taupin, Théorie dynamique de la diffraction des rayons X par les cristaux déformés, Bull. Minéral. **87**, 469 (1964).

[17] C. R. Wie, T. A. Tombrello, and T. Vreeland, Dynamical X-ray diffraction from nonuniform crystalline films: Application to X-ray rocking curve analysis, J. Appl. Phys. **59**, 3743 (1986).

[18] O. Yu. Gorobtsov and I. A. Vartanyants, Phase of transmitted wave in dynamical theory and quasi-kinematical approximation, Phys. Rev. B **93**, 184107 (2016).

[19] M. Civita, A. Diaz, R. J. Bean, A. G. Shabalin, O. Yu. Gorobtsov, I. A. Vartanyants, and I. K. Robinson, Phase modulation due to crystal diffraction by ptychographic imaging, Phys. Rev. B **97**, 104101 (2018).

[20] A. Pateras, J. Park, Y. Ahn, J. A. Tilka, M. V. Holt, H. Kim, L. J. Mawst, and P. G. Evans, Dynamical scattering in coherent hard x-ray nanobeam Bragg diffraction, Phys. Rev. B **97**, 235414 (2018).

[21] H. Yan and L. Li, X-Ray dynamical diffraction from single crystals with arbitrary shape and strain field: A universal approach to modeling, Phys. Rev. B **89**, 014104 (2014).

[22] A. G. Shabalin, O. M. Yefanov, V. L. Nosik, V. A. Bushuev, and I. A. Vartanyants, Dynamical effects in Bragg coherent x-ray diffraction imaging of finite crystals, Phys. Rev. B **96**, 064111 (2017).

[23] W. H. Richardson, Bayesian-based iterative method of image restoration, J. Opt. Soc. Am. **62**, 55 (1972).

[24] L. B. Lucy, An iterative technique for the rectification of observed distributions, Astronom. J. **79**, 745 (1974).

[25] J. N. Clark, X. Huang, R. Harder, and I. K. Robinson, High-resolution three-dimensional partially coherent diffraction imaging, Nat. Commun. **3**, 993 (2012).

[26] S. Marchesini, H. He, H. N. Chapman, S. P. Hau-Riege, A. Noy, M. R. Howells, U. Weierstall, and J. C. H. Spence, X-ray image reconstruction from a diffraction pattern alone, Phys. Rev. B **68**, 140101(R) (2003).

[27] J. Gronkowski, Propagation of X-rays in distorted crystals under dynamical diffraction, Phys. Rep. **206**, 1 (1991).

[28] O. Chubar and R. Celestre, Memory and CPU efficient computation of the Fresnel free-space propagator in Fourier optics simulations, Opt. Express **27**, 28750 (2019).

[29] R. Li and O. Chubar, in *Advances in Computational Methods for X-Ray Optics V*, edited by O. Chubar and K. Sawhney (SPIE Press, Bellingham, 2020), pp. 78–87.

[30] Q. Shen, I. Bazarov, and P. Thibault, Diffractive imaging of nonperiodic materials with future coherent x-ray sources, J. Synchrotron Rad. **11**, 432 (2004).

[31] G. Williams, M. Pfeifer, I. Vartanyants, and I. Robinson, Effectiveness of iterative algorithms in recovering phase in the presence of noise, Acta Crystallogr. A **63**, 36 (2007).